

Nanoscale

Accepted Manuscript



This is an *Accepted Manuscript*, which has been through the Royal Society of Chemistry peer review process and has been accepted for publication.

Accepted Manuscripts are published online shortly after acceptance, before technical editing, formatting and proof reading. Using this free service, authors can make their results available to the community, in citable form, before we publish the edited article. We will replace this *Accepted Manuscript* with the edited and formatted *Advance Article* as soon as it is available.

You can find more information about *Accepted Manuscripts* in the [Information for Authors](#).

Please note that technical editing may introduce minor changes to the text and/or graphics, which may alter content. The journal's standard [Terms & Conditions](#) and the [Ethical guidelines](#) still apply. In no event shall the Royal Society of Chemistry be held responsible for any errors or omissions in this *Accepted Manuscript* or any consequences arising from the use of any information it contains.

Multi-component superstructures self-assembled from nanocrystal building blocks

Rui Tan[§], Hua Zhu[§], Can Cao and Ou Chen*

Department of Chemistry, Brown University, 324 Brook St. Providence, RI 02912 (USA)

*Correspondence to: ouchen@brown.edu

Abstract:

More than three decades of intensive study in making high-quality nanocrystals have created a unique toolbox for building multi-component superstructures, which has been recognized as a new generation of metamaterials important to both fundamental sciences and applied technologies. This minireview summarizes recent advances in this exciting field. We will focus our discussion on the synthetic strategies and superstructures of this multi-component metamaterial, and highlight their novel properties and potential applications. Additionally, some perspectives on possible developments for this field are offered at the end of this review. We hope this minireview will both inform and stimulate research interests for the design and fabrication of these nanocrystal-based multi-component metamaterials for diverse applications in the future.

1. Introduction:

Multi-component superstructures (MCSs) self-assembled from more than one type of building blocks represent a new pathway for generating complex materials with potential in various technological applications.¹⁻⁴ Since the first experiments on the self-assembly of single-type nanocrystals (NCs) into superstructures in 1989⁵, inorganic NCs, with wide tunability in their size, shape and composition and easy-to-handle colloidal states, have become arguably the most popular construction material for these higher-ordered architectures.⁶⁻¹¹ However, early attempts in making MCS using NC building blocks often resulted in amorphous or short-range-ordered structures mainly due to uncontrollable driving forces, a polydispersity of the building blocks, or both.¹²⁻¹⁷ Recent advances in synthetic methods have produced NCs with an unprecedented high quality (i.e., high monodispersity, uniform morphology, and well-controlled surface state)¹⁸⁻²³, and have provided methods for controlling driving forces affecting self-assembly processes.²⁴⁻³⁰ These substantial achievements led to the ordered and programmable self-assembly of multiple types of NCs with distinct natures into complex superstructures in the nano-, meso-, and macro-scales.³¹⁻³⁶

By fine-tuning NC size ratios and concentrations, the first successful example of a long-range ordered binary-superlattice (BN-SL) self-assembled from Fe₂O₃ magnetic NCs and PbSe quantum dots (QDs) was demonstrated in 2003.⁸ Since then, this research area has truly bloomed: currently, a wide spectrum of MCSs including 2-dimensional (2D) membranes/films, 3-dimensional (3D) solids/supercrystals and high-order colloidal particles has been successfully synthesized.^{25, 34} These MCSs can not only combine or enhance the size-dependent properties of their constituents but also manifest novel interactions and synergistic properties from the near-field coupling that occurs between neighboring building blocks.^{12, 32, 37,}
38

Although there are many excellent reviews covering NC building blocks and self-assembled superstructures including synthetic methodologies, driving forces, properties and applications^{31, 32, 39-45}, a review specifically focused on the system of MCSs from colloidal inorganic NCs are few and in high demand. This minireview provides a great opportunity to summarize recent achievements in this fast-growing field. Our discussion will range from general synthetic strategies to current superstructures to highlight how MCSs have collective and synergistic properties that derive from their individual building blocks as well as their specific geometric arrangements. We will place a greater emphasis on supercrystalline superstructures with a long-range ordered periodicity. Note that template-based multi-component assemblies and heterostructure NCs synthesized through epitaxial or non-epitaxial crystal growth are generally not examined. Finally, challenges and future perspectives on this topic will conclude this review.

2. Synthetic strategies

From a general thermodynamic viewpoint, ensemble NCs arrive at equilibrium when Helmholtz free energy (F) is minimized. F is composed of two parts, the internal energy (U) and the product of temperature (T) and entropy (S). Thus, F is determined by both entropy and intermolecular forces between NCs, including van der Waals interactions⁴⁶, dipole-dipole interactions²⁴, electrostatic interactions²⁵⁻²⁷, etc.. In this section, we will describe synthetic strategies for generating MCSs broadly classified into two categories: 1) spontaneous formation mainly dependent on solvent evaporation; 2) guided formation controlled by surface chemistry.

2.1 Spontaneous formation

Spontaneous formation processes that rely on solvent evaporation represent a strategy without pre-designed interparticle interactions to guide the formation of superstructures. As solvent evaporates, the interparticle distance in solution decreases, eventually to a point where the system can undergo a transition from a disordered state to an ordered structure.^{40, 41} This can be seen as a process of minimizing total entropy,

where the gain in free volume entropy outweighs the loss in configurational entropy, thus creating an overall increase of entropy in the system.^{28, 29, 47-51} During this process, colloidal NCs can spontaneously self-assemble on certain solid substrates (e.g., alkyl-functionalized silicon chips, silicon nitride membranes or transmission electron transmission (TEM) grids), forming periodically ordered SLs.^{28, 29, 52} Murray et al. recently refined this strategy through the self-assembly of NC BN-SL membranes at a liquid/air interface.³⁵ In this procedure, a chemically inert liquid surface (e.g., diethyl glycol) substituted for solid substrates with a glass slide to control the evaporation rate (Fig. 1a). Various NCs of selected sizes and concentrations were dissolved in a low-boiling-point solvent (e.g., hexane) and then dispensed over the liquid surface. Within minutes, a floating NC-SL membrane was formed at the liquid surface as solvent evaporated (Fig. 1a). This improved method yields centimeter-scale uniform SL membranes, which are transferrable to various substrates to make NC-based devices.⁵³⁻⁵⁵

There are several parameters that can determine the superstructure from this spontaneous formation process. For instance, temperature is one of the key parameters. On one hand, with proper manipulation of temperature, one can control the solvent evaporation rate; on the other hand, as the temperature increases, entropy becomes the dominant force controlling the superstructure, favoring high packing density.²⁸ This trend was generally observed by Talapin et al. in a variety of BN NC systems.²⁹

In addition to the temperature effect, NC surface ligands also play a pivotal role when assembling to MCSs.⁵⁶⁻⁵⁸ The deformability of the hydrocarbon ligand capping layer can lead to a change in the local coordination environment, which is pivotal in BN-SL packing. An important parameter, "softness" (L/R =length of surface ligand/inorganic core radius), determines whether they will adopt the shape of a coordination environment ($L/R > 0.33$) or follow the sphere packing rules ($L/R < 0.33$).⁵⁹ Pileni et al. studied the influences of the ligand-type and showed that the assembly of NCs with different surface ligands (i.e., oleyamine and dodecanethiol) experienced a ligand exchange process.⁶⁰ This process created a large energetic penalty and affected the thermodynamic stability during assembly, leading to a remarkable change in the resulting BN structures.⁶⁰ These structures favored a kinetically trapped state with a minimum local free energy even when the packing density was low.⁶⁰

2.2 Guided formation

In contrast to the spontaneous process, specific NC surface-to-surface interactions or surface-to-solvent interactions play the dominant role in the process of guided formation of MCSs. The controlled surface interactions in recent works include the complementary interactions aided by DNA molecules and electrostatic interactions.^{26, 27, 33, 34, 61} Complementary forces from the hydrogen bonding between different bases in DNA are specifically oriented, which allows programmable engineering of DNA-based MCSs.⁶²⁻

⁶⁴ Mirkin et al. have summarized six design rules for preparing distinct colloidal crystal structures using DNA-functionalized NCs (DNA-NCs).^{34, 63} It is noted that in a BN system, the size ratio between two different DNA-NCs and the DNA linker ratio, defined as the number of linkers on two different DNA-NCs, determine the thermodynamically favored structure.³⁴

Early studies primarily focused on Au NC systems because they readily attached to alkylthiol-modified DNA strands. Mirkin et al. recently expanded this method to other NC systems by coating NCs with an azide-bearing amphiphilic polymer, which can be linked to DNA by ‘azide–alkyne click chemistry’.⁶³ Gang et al. provided an alternative strategy to form heterogeneous structures of NC-SLs by using DNA and carboxylic-based interactions.³⁸ After grafting with carboxylic groups, streptavidin was conjugated and attached to biotinylated-DNA. Four representative functional NCs can be assembled into desired superstructures using this strategy.³⁸

Aside from using DNA ligands, electrostatic interactions alone can also guide the formation of BN superstructures.^{13, 26, 65} This strategy usually relies on controlling electrostatic attraction between NCs with opposite-charged surface layers.⁶⁵ The key to this strategy lies in a balance between positively and negatively charged NCs and a proper control of the electrolyte concentration and pH.^{26, 27} Recently, Ceci et al. successfully encapsulated RNA and magnetic γ -Fe₂O₃ NCs with negatively charged cowpea chlorotic mottle virus and ferritin protein cages and formed superstructures by applying positively charged Au NCs (Fig. 1c).²⁷ The crystallinity of these structures strongly depended on Debye screening length as well as the solution pH.

Furthermore, guided MCS formation can also arise from surface-to-solvent interactions.⁶⁶⁻⁶⁹ Solvophobic interactions occurring between nonpolar ligands on NC surfaces and polar solvent molecule can be used for synthesizing colloidal superparticles (SPs).⁷⁰⁻⁷⁵ Recently, Chen et al. refined this strategy to form multi-component SPs using Fe₃O₄ NCs and CdSe/CdS core/shell QDs as building blocks.³⁶ As shown in Fig. 1d, a mixture of hydrophobic NCs was first transferred to an aqueous solution using dodecyltrimethylammonium bromide (DTAB) as a surfactant. The resulting micelle solution was injected into a poly(vinylpyrrolidone) ethylene glycol solution. The weakened van der Waals interactions between ligands and surfactants lead to the detachment of DTAB surfactants from the NC surface, introducing solvophobic interactions between ligands and solvent molecules. To minimize the total surface area and surface energy, NCs tend to aggregate to form SPs. Interestingly, a phase separation occurred inside each SP during this process. ‘Core-shell’ SPs with a magnetic NC ‘core’ and a fluorescent QD ‘shell’ were attained (Fig. 1d).³⁶

3. Diverse superstructures

Utilizing the strategies described above, a large number of MCSs with different structures and compositions have been successfully developed over the last decade. Since early observations of BN-SL self-assembly of Au and Ag NCs by Kiely et al.^{9, 76}, the library of MCSs has been continuously expanding to various systems including 2D membranes^{25, 52, 77}, 3D SL solutions^{34, 63, 78, 79}, dried solids^{26, 62, 80} and multi-component SPs.^{36, 67, 68} In this section, we will summarize this diverse structure library of MCSs with an emphasis on their supercrystallinity.

3.1 2D-SL membranes

Primarily through the spontaneous formation processes previously discussed, a wide spectrum of multi-component 2D-SLs has been achieved and demonstrated in the past ten years. Table 1 summarizes recent developments of 2D-SL membranes with different structures and building blocks. For example, Murray et al. have successfully assembled and summarized 12 different types of thermodynamically stabilized and long-range ordered BN-SLs using metal, metal oxide and semiconductor NCs (Fig. 2a-l).^{25, 52, 77} Also in their works, three ‘undefined’ BN-SLs assembled from LaF₃ triangular nanoplates and spherical NCs (Au or PbSe) and three ‘unknown’ BN-SLs assembled by Pd-PbSe, Ag-Fe₃O₄, Au-Fe₃O₄ spherical NCs have been discovered.^{25, 52} After these early studies, BN-SL membranes have expanded into various NC systems with diverse structures including isostructural NaCl⁸¹, CuAu^{82, 83}, NiAs,⁷⁹ AlB₂^{81, 82, 84}, MgZn₂^{51, 82, 84} and NaZn₁₃^{51, 81, 82, 84, 85} types. Ye et al. have carried out a more systematic study and revealed that pure bcc-AB₆ type BN-SL assembled via Fe₃O₄ and Au NCs can be formed under slow evaporation.⁸⁶ During this process, the relative phase stability of bcc-AB₆ and CaB₆ can be tailored from coexistence to phase-pure bcc-AB₆ by adjusting the NC size ratio. After early demonstration of isostructural cesium chloride (CsCl) using poly(methyl methacrylate) particles⁸⁷, the same structure has been obtained in BN-SLs from PbSe and CdSe QDs with a particle size ratio as high as 0.75.²⁸

In addition to the BN-SLs formed from a combination of metallic, magnetic and semiconductor NCs, Pileni et al., observed BN-SLs using purely metal constituents.⁸⁶ They showed the variation of size ratio of Co and Ag NCs from 1/8 to 1 will change the structure from NaZn₁₃ to a mixture of AlB₂ and AuCu, and finally to AlB₂ owing to the strong van der Waals interactions between metal NCs.^{88, 89} In contrast, using a single size ratio of inorganic cores, various of BN-SLs including new structural types such as the AB₈-type and the A₂B₃-type can be obtained by using polystyrene-grafted NCs as building blocks.⁵⁷ These polymeric ligands offer a new way to precisely tune the property of NC building blocks in more dimensions (e.g., molecular weight, chemical nature, architecture, etc.). Finally, a new structure with a [PbSe]₆[CdSe]₁₉

(A_6B_{19}) stoichiometry, which has no direct counterpart in the atomic world, has been discovered in BN-SL membranes (Fig. 2m).⁹⁰

Aside from periodic order, Archimedean tiling-based aperiodic ordering and dodecagonal quasi-crystalline (DDQC) superstructures can also be achieved by self-assembling colloidal NCs.^{30, 91, 92} For instance, Talapin et al. observed different DDQC BN-SLs assembled via intermediate NC concentration ratios following the general sphere-packing rules (Fig. 2n).⁹¹ When using ferromagnetic single domain (hcp) Co NCs instead of amorphous-phase Co particles to assemble Co-Ag BN-SLs, Pileni's group showed that the DDQC order could be obtained as a result of Co-Co magnetic dipole-dipole interactions.³⁰

In addition to spherical building blocks, multi-component membranes assembled from anisotropic shaped NCs have also been explored.^{25, 93} For example, 2D arrays of spherical NCs (i.e., Au, PbSe, Pd NCs) intercalated with parallelly aligned CdSe/CdS nanorods in the presence of suitable additive ligands were observed by Cao et al..⁹⁴ A mechanistic study suggested that spherical NCs with a high dielectric constant and a large Hamaker constant played important roles during this kinetically limited formation process. Lately, it has been demonstrated that self-assembly of NaYF₄ NRs nanorod and Fe₃O₄ nanospheres induced at the liquid-air interface could form highly ordered NC BN-SLs into several unprecedented phases including long-range ordered AB₂-type (Fig. 2o and p).⁹⁵ Three key factors have been identified for such formation, including attractive contact interactions and optimal interaction strengths as well as suitable particle geometries which allow dense packing to maximize entropic forces.⁹⁵ NCs with other shapes, such as triangular, octahedral, rhombic, tripodal and nanoplate have all been realized in SL membranes through shape complementary geometries and attractive contact interactions at optimal interaction strengths.^{96, 97}

Knowledge accumulated through studying unary and binary systems has led to several successes in making quasi-ternary and ternary-superlattice (TN-SL) membranes.^{54, 81, 98, 99} Vanmaekelbergh et al. reported the first observation of genuine TN-SLs (i.e., ABC₄) constructed from CdSe QDs and PbSe QDs of two different sizes with a maximum packing fraction as low as 0.64.⁹³ Later, bilayered ABC₂-type TN-SLs assembled from three spherical NCs and ABC-type TN-SLs assembled from small and large LaF₃ nanodisks and CdSe/CdS nanorods at a liquid-air interface were obtained by Murray et al..^{54, 98, 99} These studies further enriched the knowledge base in SL membranes and opened the doors to even more complex 2D architectures.

3.2 3D superstructures

Beyond 2D membranes, 3D MCSs research has also developed quickly within the last ten years.^{26, 100-102} While many works focused on single-component 3D SLs, various 3D MCSs including bulk SL solutions^{34, 79, 103-105}, dried nanosolids^{26, 62, 80}, and meso-scale SPs^{36, 67, 68}, have been successfully synthesized.

After early studies of applying DNA oligonucleotides as a programmable ligand to form short-range ordered assemblies^{7, 62, 80, 106, 107}, Mirkin et al. utilized these ideas in the assembly of 3D BN-SL solutions using DNA-Au NCs of different sizes as well as hollow spherical nucleic acids as “3D spacers”.^{34, 78} By independently tuning the oligonucleotide interconnection length, NC inorganic size, and NC hydrodynamic radius, 3D BN-SL isostructures with CsCl, NaCl, AlB₂, Cr₃Si, Cs₆C₆₀ were obtained.^{34, 78} Very recently, highly crystalline 3D BN-SLs have been successfully assembled by mixing two types of DNA-NCs such as CdSe/ZnS QDs, Au, Fe₃O₄ and Pt NCs with a shell of nucleic acids (Fig. 3).⁶³ Other structures, such as AB₈^{fcc}-type and AB^{sc}-type of 3D BN-SLs can be assembled by taking advantages of electrostatic forces between two oppositely charged NCs in solutions.²⁷ This concept also applies to assemblies with two types of oppositely charge proteins such as cowpea chlorotic mottle virus and amine-terminated generation six poly(amidoamine) dendrimer or cowpea chlorotic mottle virus and avidin to yield new structures (e.g., AB₁₂^{bcc}).⁶¹

Furthermore, as in 2D membrane systems, DNA assisted self-assemblies can overcome the limitations of unary and binary systems to allow the formation of 3D TN-SLs solutions.⁷⁹ Recent discoveries demonstrated a strategy of the topotactic insertion of a second component into a unary parent SL to form a BN-SL or a third component into a binary parent SL to form a TN-SL. Two unique 3D BN-SLs (A₂B₃-type and AB₄-type, both have no atomic equivalent) and three distinct 3D TN-SLs crystals structures were synthesized, such as face-perovskite type and edge-perovskite type as well as a ABC₁₂-type which has no equivalent in atomic or molecular crystals.⁷⁹ Additionally, such SL switching by intercalation has proved to be a reversible process controlled by temperature.⁷⁹

Aside from studies in 3D SL solutions, significant developments have occurred in the formation of dried nanosolids.^{26, 62, 80} Kalsin and co-workers demonstrated that mixing a solution of positively charged Au NCs and negatively charged Ag NCs coated with ω -functionalized alkane thiols will cause aggregation into binary crystals with diamond-like lattices including octahedral, truncated and twinned octahedral, truncated tetrahedral and triangular crystal morphologies.²⁶ Also, through a slow cooling of two different sizes of complementary DNA-Au NCs, rhombic dodecahedron shaped microcrystals (thermodynamically the most favorable crystal shape) with a CsCl lattice symmetry can be produced.⁶² More recently, novel 3D binary nanosolids composed of two different shapes of Au NCs were successfully assembled; examples include

cube-sphere binaries with NaCl-like lattices as shown in Fig. 4 and octahedron-sphere binaries with CsCl-like lattices.⁸⁰

3D MCSs also include meso-scale colloidal SPs. Several groups have successfully synthesized multi-component SPs using NC building blocks with different compositions including metals, metal oxides, semiconductors and lanthanides.^{67, 68, 108-110} However, producing monodispersed multi-component SPs with supercrystallinity is still a challenge. Recently, Chen et al. have developed a size-controlled synthesis of monodispersed multi-component ‘core-shell’ SPs through solvophobic interactions as previously mentioned. Additional thermal annealing treatment transformed the amorphous magnetic ‘core’ into a face-centered-cubic (fcc) supercrystalline structure, while preserving the ‘core-shell’ superstructure (Fig. 5).³⁶ Other types of multi-component SPs such as a planet-satellite structure with an Au NC surrounded by multiple QDs have also been achieved.^{111, 112} Further extensions including structures with controlled planet-satellite distances, stoichiometries, and arrangements of satellite NCs have also been reported.¹¹³⁻¹¹⁵

4. Novel properties

The fundamental advantage of assembling multi-component NCs into a single construct is the possibility of creating materials with novel and enhanced properties. These properties can be introduced from not only individual components for their size-dependent nature, but also from novel collective and synergistic properties induced by NC attachments, interparticle interactions and superstructure geometries. These enhanced functionalities make MCS materials viable in diverse areas including energy and data storage, catalysis, and biological and biomedical imaging. In this section, we will explore the number of great discoveries that have been made in this field.

4.1 Film conductivity

Inspired by the high electronic conductivity and low thermal conductivity of Ag⁺ p-doped bulk CdTe, Urban et al. have demonstrated an enhanced conductivity effect by assembling Ag₂Te and PbTe NCs into BN-SL thin films³⁷, thus overcoming the difficulty of conventional semiconductor atomic doping processes. Inside this binary film, the Ag₂Te NCs played the role of p-type nano-dopant in the PbTe NC-SL membrane. After hydrazine treatment to replace the bulky organic ligands and to decrease interparticle distances, the p-type electronic conductivity of the film showed ~100-fold enhancement in an AB BN-SL (stoichiometry ratio of 1:1), compared to films made from the individual components (Fig. 6).³⁷ This study demonstrates a clear advantage for designing and combining multi-type NCs into metamaterials.

4.2 Magnetic coupling

Strong exchange coupling and/or dipole-dipole interactions that originate from interparticle interactions and finite crystal size effects will occur inside magnetic NC assemblies. Exchange coupling effects in short-range ordered FePt-Fe₃O₄ binary nanocomposite magnets were firstly reported by Sun et al.¹² Murray et al. further improved the same system into a long-range ordered BN-SL. They showed that the AB₂-type BN-SL membranes exhibited a temperature-dependent higher magnetoresistance value than the ico-AB₁₃-type ones.¹¹⁶ This difference was attributed to their different SL structures. Based on these discoveries, a later more systematical study on magnetic thin films was carried out from the same group. They revealed that by combining magnetically hard (i.e., CoFe₂O₄) and soft (i.e., Fe₃O₄) NCs, a single-phase magnetization switching behavior can be observed at temperatures below 200K after annealing at 400°C.¹¹⁶ When annealed at a higher temperature (i.e., 500°C), NaZn₁₃-type BN-SLs exhibited a larger magnetoresistance switching field even at room temperature, which is essential for constructing nonvolatile memory chips.¹¹⁶ Furthermore, when thermally stable NCs (e.g., MnO NCs) were used to prevent the sintering of FePt NCs, the obtained BN-SL membranes were preserved even at 650 °C, which allowed the FePt NCs go through a crystal phase conversion process from superparamagnetism (fcc) to ferromagnetism (face-centered-tetragonal, fct).⁹³ This offers a new route for production of ferromagnetic NC arrays for high-density magnetic recording technology.

4.3 Catalytic activity

In addition to the enhanced conductivity and novel magnetic coupling, several groups have recently reported improved catalytic activities offered by MCS systems.^{56, 58, 96, 115, 117} Yamada et al. applied the novel concept of a ‘tandem’ bilayer of Pt and CeO₂ NCs on a silica substrate for catalysis reactions.⁵⁶ Two sequential reactions of methanol decomposition and ethylene hydroformylation were selectively catalyzed at CeO₂-Pt and Pt-SiO₂ interfaces, respectively. By assembling a variety of noble-metal NCs on metal-oxide (e.g., CeO₂ and TiO₂) NC supporting materials, mesoporous multi-component SPs can serve as thermally stable catalysts with good selectivity and robust performance for reactions at temperatures up to 500°C.¹⁰⁸ Furthermore, an excellent example showing a unique advantage of the geometric control of MCSs has been reported by Kang et al.⁹⁶ They demonstrated that Pd-Pt BN-SL electrocatalysts show 4-6 times greater activity in the oxygen reduction reaction than pure Pt octahedral NCs or a Pt-Pd NC random mixture (Fig. 7).⁹⁶ The Pd-promoted Pt catalysts were selectively assembled from 6 nm spherical Pd NCs on highly exposed (111) facets of Pt octahedral NCs in an ico-AB₁₃ BN-SL structure (Fig 4a-c). This specific binary geometry is believed to be responsible for the observed synergistic effect.⁹⁶ Thus, as demonstrated by these studies, long-range ordered supercrystalline structures represent a more efficient and customizable way to fabricate catalyst capable of high-performance and multi-functionality.

4.4 Optical and plasmonic interactions

When optical and plasmonic NCs approach each other, strong exciton and plasmonic interactions as well as synergistic phenomena are expected. Initial optical studies showed that by directly assembling Au NCs and CdSe QDs into four different types of binary superstructures, the photoluminescence of CdSe QDs dramatically decreased.⁸² This observation was attributed to the energy transfer from the exciton of QDs to the plasmon resonance of Au NCs due to the close contact between the QDs and Au NCs. Shortened QDs photoluminescence lifetime further supported this hypothesis, indicating that the radiative decay rate of the exciton was significantly influenced by the surrounding Au NCs.⁸² Later studies explored that by separating QDs from Au NCs using different spacers (e.g., DNA, organic molecule, silica, etc.), a plasmon induced photoluminescence enhancement, which has long existed at the single particle level¹¹⁸⁻¹²⁰, was observed in ensemble 3D Au NCs and QDs colloidal assemblies.^{38, 111-113, 121}

In addition to the exciton-plasmonic interactions, strong near-field plasmonic-plasmonic resonances can be achieved in BN-SLs as interparticle distances between metal NCs decrease. For the first time, Ye et al. successfully tuned the collective plasmonic response in BN-SLs self-assembled by plasmonic NCs (i.e., Au and Ag NCs), and nonplasmonic NCs (i.e., Fe₃O₄, PbS and PbTe NCs).¹²² By adjusting the NC arrangement, therefore the strength of near-field coupling between plasmonic NCs, the corresponding extinction spectra can be easily tuned across the entire visible region.

Apart from the assemblies of metal, metal oxide and semiconductor QDs, lanthanide-doped rare earth NCs (e.g., NaYF₄:Yb, Tm, Er) with upconversion emission behavior have also been used to make binary and bilayer SLs.^{54, 123} Their upconversion emissions were well-preserved in a monolayer, and superimposed in bilayer SLs without any spectrum shift, which is appealing for creating multicolor ultraviolet emission photonic devices.¹²³

4.5 Multi-functionality

Finally, a direct advantage of combining multi-type NCs is that the fabricated materials can inherit multiple functionalities from its individual components. This multi-functionality has been highlighted in colloidal binary SP systems.^{67, 124} Zhang et al. synthesized Au-Fe₃O₄ binary SPs that displayed a combined property of magnetism and catalysis, which could be potentially used as recoverable catalysts through magnetic separation and collection.⁶⁷ Similar ideas have been applied for making QD-Fe₃O₄ binary magneto-fluorescent SPs.^{68, 109, 125} Recently, Chen et al. demonstrated an excellent example of using the magneto-fluorescent 'core-shell' SPs in biological applications.³⁶ Given the ideal superstructure of a close-packed magnetic 'core', which is fully surrounded by a 'shell' of fluorescent QDs, the SPs exhibit uniform and tunable sizes, optimized fluorescent and magnetic properties, substantial colloidal stability as well as

versatile surface functionality. These features allow the obtained SPs to be magnetically manipulated inside a living cell, while being optically tracked with a high accuracy at the single-SP level (Fig. 8a-d). With desired decorations, these SPs constitute a powerful platform for the study of intracellular processes under magnetic manipulation. Moreover, given the enhanced magnetic resonance (MR) transverse relaxivity (i.e., r_2) due to the high degree of Fe_3O_4 NCs aggregation as well as their self-ordering, the SPs can also be utilized as *in vivo* MR and multiphoton dual-mode imaging probes for tumor detection and visualization at both microscopic and macroscopic scales (Fig. 8e-j).³⁶

5. Conclusion and future perspectives

In this minireview, we summarized the recent advances of NC-based MCSs. We explored the general strategies employed for synthesizing MSCs, the types of NC-based superstructures, and exciting properties of these materials. It is also noteworthy to mention that advanced techniques, including 3D tomography electron microscopy with atomic resolution^{90, 126}, external pressure treatments and a simultaneous collection of wide- and small-angle X-ray scattering^{98, 127, 128}, synchrotron-based X-ray supercrystallography¹²⁹⁻¹³², along with improved theoretical modeling and simulations have together provided a more in-depth understandings of these complicated systems from different aspects.^{62, 133, 134} Moreover, post-processing (e.g., pressure sintering), which has been recently employed for single-component superstructures¹³⁵⁻¹³⁷, can be easily transferred to well-defined MCSs to generate novel materials with undiscovered properties.

In the past decade, a significant amount of research has yielded plentiful discoveries in this rapidly growing field and potentials of MCSs have been unambiguously demonstrated. Despite this progress, limitations and challenges still remain. For example, a detailed understanding of the nucleation and growth processes of these MSCs has not been clearly demonstrated. BN- and TN-SL structures in robust and post-treatable forms have yet been reliably synthesized. Controlling the interparticle distance inside MCSs in a wide range, and scalable syntheses of these materials at a manufacturing level are both quite challenging due to the delicate synthetic procedures currently used. Moreover, properties and applications of MCSs are still been far from fully explored and studied. However, given the history of continuous progress and vast achievements in the nano-material research field, there is no doubt that these current limitations and challenges delineated by researchers will be overcome as more discoveries are made. We hope that this minireview will inspire researchers to bring multidisciplinary expertise into this young and fascinating field, and to innovatively expand the existing material-property library to push MCSs forward toward their bright future.

Table1: Summary of recent reported 2D multi-component SL superstructures:

	Isostructure/ stoichiometry	Particle shape	Building blocks (large-small NCs)	Size ratio ^a	Surface Ligand	Remarks
Binary ^{25, 52}	AB: NaCl, CuAu, Orthorhombic AB	Spherical, Triangular	Fe ₂ O ₃ -Au; PbSe-Pd	0.43*; (0.528*, 0.62*)	OA; DDT; ADA, HAD	Summary and characterizations of more than 20 types BN-SLs
	AB ₂ : AlB ₂ ,		PbSe-Ag; PbSe-Au	0.59; (0.66; 0.81)		
	MgZn ₂ , MgNi ₂		PbSe-Ag; PbS-Pd	0.71*; 0.56* ;		
	AB ₃ : Cu ₃ Au		CoPt ₃ -Fe ₂ O ₃ ; Fe ₂ O ₃ -PbSe	0.54*; 0.5*		
	AB ₄ : Fe ₄ C		PbSe-Au	0.787*		
	AB ₅ : CaCu ₅		PbSe-Pd	(0.6*; 0.48)		
	AB ₆ : CaB ₆		PbSe-Ag	0.59		
	AB ₁₃ : NaZn ₁₃ , cub-AB ₁₃		PbSe-Pd; PbSe-Ag	0.52; 0.58		
	“unknown”: 3 types ⁵²		PbSe-Ag; PbSe-Au	0.57; 0.69		
	“undefined”: 3 types ²⁵		Fe ₂ O ₃ -Au	0.37;		
Binary ³⁷	NaCl, CuAu	Spherical	PbTe-Ag ₂ Te; Ag ₂ Te-PbTe	0.49 0.64	OA, DDT	BN-SLs with enhanced p-type conductivity
	AB, AB ₂ , A ₂ B ₃ , AB ₃ ABC ₂	Spherical	Fe ₃ O ₄ -Au; Fe ₃ O ₄ -FePt ; (NaFY ₄ :Yb/Er)-Fe ₃ O ₄ Fe ₃ O ₄ - Fe ₃ O ₄ -FePt	0.44*; 0.40*; 0.49*; 0.63*; 0.42*; 1:0.48:0.37 ^b	OA	2D BN-SLs; Bilayer BN-SLs; TN-SLs
quasi- quaternary ⁵⁵	NaZn ₁₃ , AlB ₂	Spherical	(CdSe/ZnS/CdS)- (Au/Fe ₃ O ₄); (CdSe/ZnS)-(Au/Fe ₃ O ₄); (PbSe/CdSe)-(Au/Fe ₃ O ₄)	0.48 0.33 0.45	OA, OAm, HAD, DDT	Quasi-quaternary AB ₁₃ - and AB ₂ - type SLs for the first time using exclusively core/shell NCs
	NaZn ₁₃ , AlB ₂ , AuCu ₃ , bcc-AB ₆ (C ₆₀ K ₆ , C ₆₀ CS ₆)	Spherical	Fe ₃ O ₄ -Polymer-grafted Au	0.49*	OA, TP, CP	10 different BN-SLs formed by polymer- grafted NCs
	NaCl, MgZn ₂ , CaCu ₅ , AB ₈ , AB(CsCl), A ₂ B ₃			0.49*		
	0.40* 0.69* 0.49*					
Binary ⁶⁰	NaCl, AlB ₂ , NaZn ₁₃ , MgZn ₂	Spherical	Au,(w/different sizes)	0.43*; 0.57* 0.57*; 0.82*	OAm	Ligand coverage, solvent type, dependent stability
Polymorphism Binary ⁷⁷	ico-AB ₁₃ , cub-AB ₁₃	Spherical	PbSe-Pd Fe ₃ O ₄ -PbSe	0.627*; 0.671*; 0.595* 0.520*	OA, DDT	Identify AB ₁₃ polymorph
Quasi-ternary ⁸¹	NaCl, NiAs, AlB ₂ , AB ₁₃ , NaZn ₁₃ , cub-AB ₁₃	Spherical	Fe/Fe ₃ O ₄ (core/shell)-Au	0.44*	OA, OAm	TN-SLs with high packing density
Binary ⁸⁴	AlB ₂ , MgZn ₂ , CaCu ₅ , cub-NaZn ₁₃ , ico-NaZn ₁₃	Spherical	CdTe-CdSe CdTe-Au	0.57*, 0.63* 0.71*, 0.81*	DDT	Size ratio dependent BN- SLs
Binary ⁸⁵	AB ₂ , cub-AB ₁₃	Spherical	PbSe-CdSe	0.56*	TOPO, HDA, OA	QD BN-SLs
Binary ⁸⁶	CaB ₆ , bcc-AB ₆	Spherical	Fe ₃ O ₄ -Au	0.43*	DDT	Identify AB ₆ polymorph
Binary ⁸⁸	NaCl, AlB ₂ , AuCu, AuCu ₃ , NaZn ₁₃	Spherical	Co-Ag	0.49*; 0.49*~0.59*; 0.54*~0.67*	OA, DDT	Conc. ratio led to structure change

Binary ⁸⁹	MgZn ₂ , NaZn ₁₃	Spherical	Co-Co; Co-Ag	0.76* ; 0.59*	OA, DDT	Magnetic Dipolar Interactions
Binary ⁹⁰	A ₆ B ₁₉ : [PbSe] ₆ [CdSe] ₁₉	Spherical	PbSe-CdSe	0.61~0.67	OA, HDA	New structure, A ₆ B ₁₉ -type
Quasi-Binary ⁹¹	AB _{3.86} -type	Spherical	PbS-Pd, Fe ₂ O ₃ -Au	0.43*	OA, DDT	Identification of quasicrystalline order BN-SLs
Binary ⁹⁵	AB ₂ -type	Rod, Spherical	NaYF ₄ -Fe ₃ O ₄ ; CdSe-Au; NaYF ₄ -UO ₂ ; CdSe-Pd	(0.56,0.29) ^c ; (1.12,0.32) (0.38,0.19); (0.92,0.26)	OA,	Formation of AB ₂ BN-SLs with NCs of Rod and spherical shape
Binary; Ternary ⁹⁸	AC ₂ : AlB ₂ BC ₂ : MgZn ₂ ABC ₄ : AlMgB ₄	Spherical	PbSe-CdSe PbSe-CdSe PbSe-PbSe-CdSe	0.48 0.73 1:0.65:0.48	OA, HDA	Observation of a TN-SLs with ABC ₄ -type
Binary, Ternary ⁹⁹	AB, AB ₂ , AB ₆ , ABC	Disk, Rod	LaF ₃ -(CdSe/CdS) LaF ₃ -LaF ₃ -(CdSe/CdS)	0.40* 0.25* 1:0.40:0.25*	OA	BN-SLs and TN-SLs with NCs of Disk and Rod shape
Binary ¹¹⁶	NaZn ₁₃ , MgZn ₂	Spherical	CoFe ₂ O ₄ -Fe ₃ O ₄	0.53; 0.74	OA	BN-SLs with bistable magnetoresistance switching behavior
Binary ¹³⁸	ico-AB ₁₃	Spherical	Silica (15nm, 29.1nm)	0.52	--	Silica BN-SLs
Binary ¹³⁹	NaCl, CaCu ₅ , AlB ₂ , NaZn ₁₃ , bcc-AB ₆ , quasicrystals	Spherical	{Mo ₁₃₂ }-PbS ^d ; {Mo ₁₃₂ }-CdSe ^e ; {Mo ₁₃₂ }-PbS/CdS); {Mo ₇₂ V ₃₀ }-PbS	(0.41*,0.51*, 0.58*,0.74*) ^d 0.49* ^e 0.46* ^e 0.68* ^e	DDA, OA	POM/NC BN-SLs
Binary ¹⁴⁰	AB	Spherical	Mo ₁₃₂ - (γ-Fe ₃ O ₄)	0.63*	DDA, DODA, OA	BN-SLs preserving magnetic properties
Binary ¹⁴¹	NaZn ₁₃ , CsCl	Spherical	Co-Ag	0.73	OA, DDT	CoAu ₁₃ BN-SLs with high thermal stability
Binary ¹⁴²	AB ₆	Spherical	Fe ₃ O ₄ -PbSe	0.32	OA	BN-SLs formed via controlled fusion of hexamer NC clusters
Binary ¹⁴³	Simple hexagonal AB ₂	Spherical	Si-Au	0.527*	DD, DDT	First Au/Si BN-SLs

*: Effective size ratio.

^a: NC size ratio, small/large;

^b: Determined by $d_{\text{eff}} = d_{\text{core}} + 2d_{\text{shell}}$, size ratio $\gamma = d_{\text{small}}/d_{\text{large}}$.⁵⁴

^c: Size ratio indicates by (diameter of sphere/diameter of Rod, diameter of sphere/length of Rod).

^d: All five structures and quasicrystals can be formed for {Mo₁₃₂}-PbS with $\gamma = 0.41 \sim 0.74$;

^e: AlB₂, NaZn₁₃, and quasicrystal can be formed for {Mo₁₃₂}-CdSe with $\gamma = 0.49$; AlB₂ structure formed for {Mo₁₃₂}-PbS/CdS with $\gamma = 0.46$ and for {Mo₇₂V₃₀}-PbS with $\gamma = 0.68$.

DDA: dioctadecyldimethylammonium; **TOPO**: trioctylphosphine oxide; **DD**: dodecene.

OA: oleic acid; **DDT**: dodecanethiol; **HDA**: hexadecylamine; **DDA**: dodecyldimethylammonium;

POM: polyoxometalate clusters; **TP**: thiol-terminated polystyrenes; **CP**: carboxyl-terminated polystyrenes.

References:

1. Gibson, R.F. A review of recent research on mechanics of multifunctional composite materials and structures. *Compos Struct* **92**, 2793-2810 (2010).
2. Suh, W.H., Suh, Y.H. & Stucky, G.D. Multifunctional nanosystems at the interface of physical and life sciences. *Nano Today* **4**, 27-36 (2009).
3. Bigall, N.C., Parak, W.J. & Dorfs, D. Fluorescent, magnetic and plasmonic-Hybrid multifunctional colloidal nano objects. *Nano Today* **7**, 282-296 (2012).
4. Lee, J.E., Lee, N., Kim, T., Kim, J. & Hyeon, T. Multifunctional Mesoporous Silica Nanocomposite Nanoparticles for Theranostic Applications. *Accounts Chem Res* **44**, 893-902 (2011).
5. Bentzon, M.D., Vanwonderghem, J., Morup, S., Tholen, A. & Koch, C.J.W. Ordered Aggregates of Ultrafine Iron-Oxide Particles - Super Crystals. *Philos Mag B* **60**, 169-178 (1989).
6. Shenton, W., Pum, D., Sleytr, U.B. & Mann, S. Synthesis of cadmium sulphide superlattices using self-assembled bacterial S-layers. *Nature* **389**, 585-587 (1997).
7. Park, S.Y. et al. DNA-programmable nanoparticle crystallization. *Nature* **451**, 553-556 (2008).
8. Redl, F.X., Cho, K.S., Murray, C.B. & O'Brien, S. Three-dimensional binary superlattices of magnetic nanocrystals and semiconductor quantum dots. *Nature* **423**, 968-971 (2003).
9. Kiely, C.J., Fink, J., Brust, M., Bethell, D. & Schiffrin, D.J. Spontaneous ordering of bimodal ensembles of nanoscopic gold clusters. *Nature* **396**, 444-446 (1998).
10. Saunders, A.E. & Korgel, B.A. Observation of an AB phase in bidisperse nanocrystal superlattices. *Chemphyschem* **6**, 61-65 (2005).
11. Glotzer, S.C. & Solomon, M.J. Anisotropy of building blocks and their assembly into complex structures. *Nat Mater* **6**, 557-562 (2007).
12. Zeng, H., Li, J., Liu, J.P., Wang, Z.L. & Sun, S.H. Exchange-coupled nanocomposite magnets by nanoparticle self-assembly. *Nature* **420**, 395-398 (2002).
13. Kolny, J., Kornowski, A. & Weller, H. Self-organization of cadmium sulfide and gold nanoparticles by electrostatic interaction. *Nano Lett* **2**, 361-364 (2002).
14. Galow, T.H., Boal, A.K. & Rotello, V.M. A "Building Block" Approach to Mixed-Colloid Systems Through Electrostatic Self-Organization. *Adv. Mater.* **12**, 576-579 (2000).
15. Hao, E.C. et al. Assembly of alternating TiO₂/CdS nanoparticle composite films. *J. Mater. Chem.* **8**, 1327-1328 (1998).
16. Gomez, S. et al. Platinum colloids stabilized by bifunctional ligands: self-organization and connection to gold. *Chem Commun*, 1474-1475 (2001).
17. Fullam, S., Rensmo, H., Rao, S.N. & Fitzmaurice, D. Noncovalent self-assembly of silver and gold nanocrystal aggregates in solution. *Chem Mater* **14**, 3643-3650 (2002).
18. Park, J., Joo, J., Kwon, S.G., Jang, Y. & Hyeon, T. Synthesis of monodisperse spherical nanocrystals. *Angew Chem Int Edit* **46**, 4630-4660 (2007).
19. Reiss, P., Protiere, M. & Li, L. Core/Shell Semiconductor Nanocrystals. *Small* **5**, 154-168 (2009).
20. Park, J. et al. Ultra-large-scale syntheses of monodisperse nanocrystals. *Nat Mater* **3**, 891-895 (2004).
21. Chen, O. et al. Compact high-quality CdSe-CdS core-shell nanocrystals with narrow emission linewidths and suppressed blinking. *Nat Mater* **12**, 445-451 (2013).
22. Chen, O., Wei, H., Maurice, A., Bawendi, M. & Reiss, P. Pure colors from core-shell quantum dots. *MRS Bulletin* **38**, 696-702 (2013).
23. Tan, R. et al. Reducing Competition by Coordinating Solvent Promotes Morphological Control in Alternating Layer Growth of CdSe/CdS Core/Shell Quantum Dots. *Chem Mater* **27**, 7468-7480 (2015).
24. Lalatonne, Y., Richardi, J. & Pileni, M.P. Van der Waals versus dipolar forces controlling mesoscopic organizations of magnetic nanocrystals. *Nat Mater* **3**, 121-125 (2004).

25. Shevchenko, E.V., Talapin, D.V., Kotov, N.A., O'Brien, S. & Murray, C.B. Structural diversity in binary nanoparticle superlattices. *Nature* **439**, 55-59 (2006).
26. Kalsin, A.M. et al. Electrostatic self-assembly of binary nanoparticle crystals with a diamond-like lattice. *Science* **312**, 420-424 (2006).
27. Kostianen, M.A. et al. Electrostatic assembly of binary nanoparticle superlattices using protein cages. *Nat Nanotechnol* **8**, 52-56 (2013).
28. Evers, W.H. et al. Entropy-driven formation of binary semiconductor-nanocrystal superlattices. *Nano Lett* **10**, 4235-4241 (2010).
29. Bodnarchuk, M.I., Kovalenko, M.V., Heiss, W. & Talapin, D.V. Energetic and entropic contributions to self-assembly of binary nanocrystal superlattices: temperature as the structure-directing factor. *J Am Chem Soc* **132**, 11967-11977 (2010).
30. Yang, Z., Wei, J., Bonville, P. & Pileni, M.P. Beyond entropy: magnetic forces induce formation of quasicrystalline structure in binary nanocrystal superlattices. *J Am Chem Soc* **137**, 4487-4493 (2015).
31. Lu, Z.D. & Yin, Y.D. Colloidal nanoparticle clusters: functional materials by design. *Chem Soc Rev* **41**, 6874-6887 (2012).
32. Wang, T., LaMontagne, D., Lynch, J., Zhuang, J.Q. & Cao, Y.C. Colloidal superparticles from nanoparticle assembly. *Chem Soc Rev* **42**, 2804-2823 (2013).
33. Nykypanchuk, D., Maye, M.M., van der Lelie, D. & Gang, O. DNA-guided crystallization of colloidal nanoparticles. *Nature* **451**, 549-552 (2008).
34. Macfarlane, R.J. et al. Nanoparticle Superlattice Engineering with DNA. *Science* **334**, 204-208 (2011).
35. Dong, A.G., Chen, J., Vora, P.M., Kikkawa, J.M. & Murray, C.B. Binary nanocrystal superlattice membranes self-assembled at the liquid-air interface. *Nature* **466**, 474-477 (2010).
36. Chen, O. et al. Magneto-Fluorescent Core-Shell Supernanoparticles. *Nat Commun* **5**, 5093 (2014).
37. Urban, J.J., Talapin, D.V., Shevchenko, E.V., Kagan, C.R. & Murray, C.B. Synergism in binary nanocrystal superlattices leads to enhanced p-type conductivity in self-assembled PbTe/Ag₂Te thin films. *Nat Mater* **6**, 115-121 (2007).
38. Zhang, Y., Lu, F., Yager, K.G., van der Lelie, D. & Gang, O. A general strategy for the DNA-mediated self-assembly of functional nanoparticles into heterogeneous systems. *Nat Nanotechnol* **8**, 865-872 (2013).
39. Talapin, D.V., Lee, J.S., Kovalenko, M.V. & Shevchenko, E.V. Prospects of Colloidal Nanocrystals for Electronic and Optoelectronic Applications. *Chem Rev* **110**, 389-458 (2010).
40. Nie, Z., Petukhova, A. & Kumacheva, E. Properties and emerging applications of self-assembled structures made from inorganic nanoparticles. *Nat Nanotechnol* **5**, 15-25 (2010).
41. Kovalenko, M.V. et al. Prospects of Nanoscience with Nanocrystals. *ACS Nano* **9**, 1012-1057 (2015).
42. Hanrath, T. Colloidal nanocrystal quantum dot assemblies as artificial solids. *J Vac Sci Technol A* **30**, 030802 (2012).
43. Wang, C.Y., Siu, C., Zhang, J. & Fang, J.Y. Understanding the forces acting in self-assembly and the implications for constructing three-dimensional (3D) supercrystals. *Nano Res* **8**, 2445-2466 (2015).
44. Luo, D., Yan, C. & Wang, T. Interparticle Forces Underlying Nanoparticle Self-Assemblies. *Small* **11**, 5984-6008 (2015).
45. Quan, Z.W. & Fang, J.Y. Superlattices with non-spherical building blocks. *Nano Today* **5**, 390-411 (2010).
46. Ohara, P.C., Leff, D.V., Heath, J.R. & Gelbart, W.M. Crystallization of opals from polydisperse nanoparticles. *Phys Rev Lett* **75**, 3466-3469 (1995).
47. Eldridge, M.D., Madden, P.A. & Frenkel, D. Entropy-driven formation of a superlattice in hardsphere binary mixture. *Nature* **365**, 35-37 (1993).

48. Cottin, X. & Monson, P.A. Substitutionally Ordered Solid-Solutions of Hard-Spheres. *J. Chem. Phys.* **102**, 3354-3360 (1995).
49. Bolhuis, P.G., Frenkel, D., Mau, S.C. & Huse, D.A. Entropy difference between crystal phases. *Nature* **388**, 235-236 (1997).
50. Trizac, E., Eldridge, M.D. & Madden, P.A. Stability of the AB crystal for asymmetric binary hard sphere mixtures. *Mol Phys* **90**, 675-678 (1997).
51. Chen, Z., Moore, J., Radtke, G., Siringhaus, H. & O'Brien, S. Binary nanoparticle superlattices in the semiconductor-semiconductor system: CdTe and CdSe. *J Am Chem Soc* **129**, 15702-15709 (2007).
52. Shevchenko, E.V., Talapin, D.V., Murray, C.B. & O'Brien, S. Structural characterization of self-assembled multifunctional binary nanoparticle superlattices. *J Am Chem Soc* **128**, 3620-3637 (2006).
53. Dong, A., Chen, J., Ye, X., Kikkawa, J.M. & Murray, C.B. Enhanced thermal stability and magnetic properties in NaCl-type FePt-MnO binary nanocrystal superlattices. *J Am Chem Soc* **133**, 13296-13299 (2011).
54. Dong, A., Ye, X., Chen, J. & Murray, C.B. Two-dimensional binary and ternary nanocrystal superlattices: the case of monolayers and bilayers. *Nano Lett* **11**, 1804-1809 (2011).
55. Cargnello, M., Diroll, B.T., Gauldin, E.A. & Murray, C.B. Enhanced energy transfer in quasi-quaternary nanocrystal superlattices. *Adv Mater* **26**, 2419-2423 (2014).
56. Yamada, Y. et al. Nanocrystal bilayer for tandem catalysis. *Nat Chem* **3**, 372-376 (2011).
57. Ye, X. et al. Structural diversity in binary superlattices self-assembled from polymer-grafted nanocrystals. *Nat Commun* **6**, 10052 (2015).
58. Li, P., Wei, Z., Wu, T., Peng, Q. & Li, Y. Au-ZnO hybrid nanopyramids and their photocatalytic properties. *J Am Chem Soc* **133**, 5660-5663 (2011).
59. Boles, M.A. & Talapin, D.V. Many-body effects in nanocrystal superlattices: departure from sphere packing explains stability of binary phases. *J Am Chem Soc* **137**, 4494-4502 (2015).
60. Wei, J., Schaeffer, N. & Pileni, M.P. Ligand Exchange Governs the Crystal Structures in Binary Nanocrystal Superlattices. *J Am Chem Soc* **137**, 14773-14784 (2015).
61. Liljestrom, V., Mikkila, J. & Kostiaainen, M.A. Self-assembly and modular functionalization of three-dimensional crystals from oppositely charged proteins. *Nat Commun* **5**, 4445 (2014).
62. Auyeung, E. et al. DNA-mediated nanoparticle crystallization into Wulff polyhedra. *Nature* **505**, 73-77 (2014).
63. Zhang, C. et al. A general approach to DNA-programmable atom equivalents. *Nat Mater* **12**, 741-746 (2013).
64. Zhang, Y. et al. Selective transformations between nanoparticle superlattices via the reprogramming of DNA-mediated interactions. *Nat Mater* **14**, 840-847 (2015).
65. Zhang, S., Shao, Y.Y., Yin, G.P. & Lin, Y.H. Electrostatic Self-Assembly of a Pt-around-Au Nanocomposite with High Activity towards Formic Acid Oxidation. *Angew Chem Int Edit* **49**, 2211-2214 (2010).
66. Bai, F. et al. A versatile bottom-up assembly approach to colloidal spheres from nanocrystals. *Angew Chem Int Edit* **46**, 6650-6653 (2007).
67. Zhang, X. et al. Binary superparticles from preformed Fe₃O₄ and Au nanoparticles. *Crystengcomm* **13**, 5674-5676 (2011).
68. Han, J.S. et al. Fabrication of CdTe nanoparticles-based superparticles for an improved detection of Cu²⁺ and Ag⁺. *J. Mater. Chem.* **22**, 2679-2686 (2012).
69. Lu, Z.D., Ye, M.M., Li, N., Zhong, W.W. & Yin, Y.D. Self-Assembled TiO₂ Nanocrystal Clusters for Selective Enrichment of Intact Phosphorylated Proteins. *Angew Chem Int Edit* **49**, 1862-1866 (2010).
70. Zhuang, J.Q., Wu, H.M., Yang, Y.G. & Cao, Y.C. Controlling colloidal superparticle growth through solvophobic interactions. *Angew Chem Int Edit* **47**, 2208-2212 (2008).

71. Zhuang, J., Wu, H., Yang, Y. & Cao, Y.C. Supercrystalline colloidal particles from artificial atoms. *J Am Chem Soc* **129**, 14166-14167 (2007).
72. Zhuang, J. et al. Cylindrical superparticles from semiconductor nanorods. *J Am Chem Soc* **131**, 6084-6085 (2009).
73. Wang, T. et al. Self-Assembled Colloidal Superparticles from Nanorods. *Science* **338**, 358-363 (2012).
74. Yang, Z. et al. Supracrystalline Colloidal Eggs: Epitaxial Growth and Freestanding Three-Dimensional Supracrystals in Nanoscaled Colloidosomes. *J Am Chem Soc* **138**, 3493-3500 (2016).
75. Wei, J. et al. Yolk/Shell Assembly of Gold Nanoparticles by Size Segregation in Solution. *J Am Chem Soc* **138**, 3274-3277 (2016).
76. Kiely, C.J. et al. Ordered colloidal nanoalloys. *Adv. Mater.* **12**, 640-643 (2000).
77. Shevchenko, E.V., Talapin, D.V., O'Brien, S. & Murray, C.B. Polymorphism in AB₁₃ Nanoparticle Superlattices An Example of Semiconductor-Metal Metamaterials. *J. Am. Chem. Soc.* **127**, 8741-8747 (2005).
78. Auyeung, E. et al. Synthetically programmable nanoparticle superlattices using a hollow three-dimensional spacer approach. *Nat Nanotechnol* **7**, 24-28 (2012).
79. Macfarlane, R.J., Jones, M.R., Lee, B., Auyeung, E. & Mirkin, C.A. Topotactic Interconversion of Nanoparticle Superlattices. *Science* **341**, 1222-1225 (2013).
80. Lu, F., Yager, K.G., Zhang, Y., Xin, H. & Gang, O. Superlattices assembled through shape-induced directional binding. *Nat Commun* **6**, 6912 (2015).
81. Shevchenko, E.V., Kortright, J.B., Talapin, D.V., Aloni, S. & Alivisatos, A.P. Quasi-ternary nanoparticle superlattices through nanoparticle design. *Adv. Mater.* **19**, 4183-4188 (2007).
82. Shevchenko, E.V. et al. Self-assembled binary superlattices of CdSe and Au nanocrystals and their fluorescence properties. *J Am Chem Soc* **130**, 3274-+ (2008).
83. Lu, C., Chen, Z. & O'Brien, S. Optimized conditions for the self-organization of CdSe-Au and CdSe-CdSe binary nanoparticle superlattices. *Chem Mater* **20**, 3594-3600 (2008).
84. Chen, Z. & O'Brien, S. Structure direction of II-VI semiconductor quantum dot binary nanoparticle superlattices by tuning radius ratio. *ACS Nano* **2**, 1219-1229 (2008).
85. Overgaag, K. et al. Binary superlattices of PbSe and CdSe nanocrystals. *J Am Chem Soc* **130**, 7833-7835 (2008).
86. Ye, X., Chen, J. & Murray, C.B. Polymorphism in self-assembled AB₆ binary nanocrystal superlattices. *J Am Chem Soc* **133**, 2613-2620 (2011).
87. Schofield, A.B. Binary hard-sphere crystals with the cesium chloride structure. *Phys Rev E Stat Nonlin Soft Matter Phys* **64**, 051403 (2001).
88. Yang, Z., Wei, J. & Pileni, M.-P. Metal-Metal Binary Nanoparticle Superlattices: A Case Study of Mixing Co and Ag Nanoparticles. *Chem Mater* **27**, 2152-2157 (2015).
89. Yang, Z.J., Wei, J.J., Bonville, P. & Pileni, M.P. Engineering the Magnetic Dipolar Interactions in 3D Binary Supracrystals Via Mesoscale Alloying. *Adv Funct Mater* **25**, 4908-4915 (2015).
90. Boneschanscher, M.P. et al. Electron tomography resolves a novel crystal structure in a binary nanocrystal superlattice. *Nano Lett* **13**, 1312-1316 (2013).
91. Talapin, D.V. et al. Quasicrystalline order in self-assembled binary nanoparticle superlattices. *Nature* **461**, 964-967 (2009).
92. Bodnarchuk, M.I., Shevchenko, E.V. & Talapin, D.V. Structural defects in periodic and quasicrystalline binary nanocrystal superlattices. *J Am Chem Soc* **133**, 20837-20849 (2011).
93. Sanchez-Iglesias, A., Grzelczak, M., Perez-Juste, J. & Liz-Marzan, L.M. Binary self-assembly of gold nanowires with nanospheres and nanorods. *Angew Chem Int Ed Engl* **49**, 9985-9989 (2010).
94. Nagaoka, Y., Wang, T., Lynch, J., LaMontagne, D. & Cao, Y.C. Binary assembly of colloidal semiconductor nanorods with spherical metal nanoparticles. *Small* **8**, 843-846 (2012).
95. Ye, X. et al. Shape alloys of nanorods and nanospheres from self-assembly. *Nano Lett* **13**, 4980-4988 (2013).

96. Kang, Y. et al. Design of Pt-Pd binary superlattices exploiting shape effects and synergistic effects for oxygen reduction reactions. *J Am Chem Soc* **135**, 42-45 (2013).
97. Paik, T. & Murray, C.B. Shape-directed binary assembly of anisotropic nanoplates: a nanocrystal puzzle with shape-complementary building blocks. *Nano Lett* **13**, 2952-2956 (2013).
98. Evers, W.H., Friedrich, H., Fillion, L., Dijkstra, M. & Vanmaekelbergh, D. Observation of a ternary nanocrystal superlattice and its structural characterization by electron tomography. *Angew Chem Int Ed Engl* **48**, 9655-9657 (2009).
99. Paik, T., Diroll, B.T., Kagan, C.R. & Murray, C.B. Binary and ternary superlattices self-assembled from colloidal nanodisks and nanorods. *J Am Chem Soc* **137**, 6662-6669 (2015).
100. Podsiadlo, P. et al. The role of order, nanocrystal size, and capping ligands in the collective mechanical response of three-dimensional nanocrystal solids. *J Am Chem Soc* **132**, 8953-8960 (2010).
101. Rupich, S.M., Shevchenko, E.V., Bodnarchuk, M.I., Lee, B. & Talapin, D.V. Size-dependent multiple twinning in nanocrystal superlattices. *J Am Chem Soc* **132**, 289-296 (2010).
102. Compton, O.C. & Osterloh, F.E. Evolution of size and shape in the colloidal crystallization of gold nanoparticles. *J Am Chem Soc* **129**, 7793-7798 (2007).
103. Jones, M.R. et al. DNA-nanoparticle superlattices formed from anisotropic building blocks. *Nat Mater* **9**, 913-917 (2010).
104. Radha, B. et al. Reconstitutable nanoparticle superlattices. *Nano Lett* **14**, 2162-2167 (2014).
105. Ross, M.B., Ku, J.C., Vaccarezza, V.M., Schatz, G.C. & Mirkin, C.A. Nanoscale form dictates mesoscale function in plasmonic DNA-nanoparticle superlattices. *Nat Nanotechnol* **10**, 453-458 (2015).
106. Mirkin, C.A., Letsinger, R.L., Mucic, R.C. & Storhoff, J.J. A DNA-based method for rationally assembling nanoparticles into macroscopic materials. *Nature* **382**, 607-609 (1996).
107. Park, S.J., Lazarides, A.A., Storhoff, J.J., Pesce, L. & Mirkin, C.A. The structural characterization of oligonucleotide-modified gold nanoparticle networks formed by DNA hybridization. *J Phys Chem B* **108**, 12375-12380 (2004).
108. Chen, C. et al. Mesoporous multicomponent nanocomposite colloidal spheres: ideal high-temperature stable model catalysts. *Angew Chem Int Ed Engl* **50**, 3725-3729 (2011).
109. Ortgies, D.H. et al. In Vivo Deep Tissue Fluorescence and Magnetic Imaging Employing Hybrid Nanostructures. *ACS Appl Mater Interfaces* **8**, 1406-1414 (2016).
110. Zhang, Q., Wang, X. & Zhu, Y. Multicolor upconverted luminescence-encoded superparticles via controlling self-assembly based on hydrophobic lanthanide-doped NaYF₄ nanocrystals. *J. Mater. Chem.* **21**, 12132-12138 (2011).
111. Nepal, D., Drummy, L.F., Biswas, S., Park, K. & Vaia, R.A. Large Scale Solution Assembly of Quantum Dot–Gold Nanorod Architectures with Plasmon Enhanced Fluorescence. *ACS Nano* **7**, 9064-9074 (2013).
112. Cohen-Hoshen, E., Bryant, G.W., Pinkas, I., Sperling, J. & Bar-Joseph, I. Exciton-plasmon interactions in quantum dot-gold nanoparticle structures. *Nano Lett* **12**, 4260-4264 (2012).
113. Sun, D.Z. et al. Light-Harvesting Nanoparticle Core-Shell Clusters with Controllable Optical Output. *ACS Nano* **9**, 5657-5665 (2015).
114. Schreiber, R. et al. Hierarchical assembly of metal nanoparticles, quantum dots and organic dyes using DNA origami scaffolds. *Nat Nanotechnol* **9**, 74-78 (2014).
115. Ma, K., Yehezkeli, O., Domaille, D.W., Funke, H.H. & Cha, J.N. Enhanced Hydrogen Production from DNA-Assembled Z-Scheme TiO₂-CdS Photocatalyst Systems. *Angew Chem Int Edit* **54**, 11490-11494 (2015).
116. Chen, J. et al. Bistable magnetoresistance switching in exchange-coupled CoFe₂O₄-Fe₃O₄ binary nanocrystal superlattices by self-assembly and thermal annealing. *ACS Nano* **7**, 1478-1486 (2013).
117. Kang, Y. et al. Engineering catalytic contacts and thermal stability: gold/iron oxide binary nanocrystal superlattices for CO oxidation. *J Am Chem Soc* **135**, 1499-1505 (2013).

118. Dey, S. et al. An experimental and theoretical mechanistic study of biexciton quantum yield enhancement in single quantum dots near gold nanoparticles. *Nanoscale* **7**, 6851-6858 (2015).
119. Ji, B. et al. Non-blinking quantum dot with a plasmonic nanoshell resonator. *Nat Nanotechnol* **10**, 170-175 (2015).
120. Shimizu, K.T., Woo, W.K., Fisher, B.R., Eisler, H.J. & Bawendi, M.G. Surface-enhanced emission from single semiconductor nanocrystals. *Phys Rev Lett* **89**, 117401 (2002).
121. Li, X., Kao, F.J., Chuang, C.C. & He, S. Enhancing fluorescence of quantum dots by silica-coated gold nanorods under one- and two-photon excitation. *Opt Express* **18**, 11335-11346 (2010).
122. Ye, X., Chen, J., Diroll, B.T. & Murray, C.B. Tunable plasmonic coupling in self-assembled binary nanocrystal superlattices studied by correlated optical microspectrophotometry and electron microscopy. *Nano Lett* **13**, 1291-1297 (2013).
123. Zheng, T. et al. Construction of NaREF₄-based binary and bilayer nanocrystal assemblies. *Chem Commun* **49**, 5799-5801 (2013).
124. Yang, G.L., Zhong, H.Z., Liu, R.B., Li, Y.F. & Zou, B.S. In Situ Aggregation of ZnSe Nanoparticles into Supraparticles: Shape Control and Doping Effects. *Langmuir* **29**, 1970-1976 (2013).
125. Sun, X.Y. et al. Bifunctional Superparticles Achieved by Assembling Fluorescent CuInS₂@ZnS Quantum Dots and Amphibious Fe₃O₄ Nanocrystals. *J Phys Chem C* **117**, 21014-21020 (2013).
126. Bals, S., Goris, B., Liz-Marzan, L.M. & Van Tendeloo, G. Three-dimensional characterization of noble-metal nanoparticles and their assemblies by electron tomography. *Angew Chem Int Ed Engl* **53**, 10600-10610 (2014).
127. Wu, H., Wang, Z. & Fan, H. Stress-induced nanoparticle crystallization. *J Am Chem Soc* **136**, 7634-7636 (2014).
128. Wang, Z. et al. Integrating in situ high pressure small and wide angle synchrotron x-ray scattering for exploiting new physics of nanoparticle supercrystals. *Rev Sci Instrum* **81**, 093902 (2010).
129. Wang, Z. et al. Correlating superlattice polymorphs to internanoparticle distance, packing density, and surface lattice in assemblies of PbS nanoparticles. *Nano Lett* **13**, 1303-1311 (2013).
130. Li, R., Bian, K., Hanrath, T., Bassett, W.A. & Wang, Z. Decoding the superlattice and interface structure of truncate PbS nanocrystal-assembled supercrystal and associated interaction forces. *J Am Chem Soc* **136**, 12047-12055 (2014).
131. Qiu, Y. et al. Microfluidic-based fabrication, characterization and magnetic functionalization of microparticles with novel internal anisotropic structure. *Sci Rep-Uk* **5** (2015).
132. Li, R. et al. Competing Interactions between Various Entropic Forces toward Assembly of Pt₃Ni Octahedra into a Body-Centered Cubic Superlattice. *Nano Lett* (2016).
133. Damasceno, P.F., Engel, M. & Glotzer, S.C. Predictive Self-Assembly of Polyhedra into Complex Structures. *Science* **337**, 453-457 (2012).
134. Khadilkar, M.R. & Escobedo, F.A. Heuristic rule for binary superlattice coassembly: mixed plastic mesophases of hard polyhedral nanoparticles. *Phys Rev Lett* **113**, 165504 (2014).
135. Wu, H. et al. Nanostructured Gold Architectures Formed through High Pressure-Driven Sintering of Spherical Nanoparticle Arrays. *J Am Chem Soc* **132**, 12826-12828 (2010).
136. Wang, Z. et al. Deviatoric stress driven formation of large single-crystal PbS nanosheet from nanoparticles and in situ monitoring of oriented attachment. *J Am Chem Soc* **133**, 14484-14487 (2011).
137. Wang, T. et al. Pressure Processing of Nanocube Assemblies Toward Harvesting of a Metastable PbS Phase. *Adv Mater* **27**, 4544-4549 (2015).
138. Sakamoto, Y. et al. Electron Microscopy Study of Binary Nanocolloidal Crystals with ico-AB₁₃ Structure Made of Monodisperse Silica Nanoparticles. *J. Phys. Chem. C* **118**, 15004-15010 (2014).
139. Bodnarchuk, M.I., Erni, R., Krumeich, F. & Kovalenko, M.V. Binary superlattices from colloidal nanocrystals and giant polyoxometalate clusters. *Nano Lett* **13**, 1699-1705 (2013).

140. Breitwieser, R. et al. Binary Superlattices from $\{\text{Mo}_{132}\}$ Polyoxometalates and Maghemite Nanocrystals: Long-Range Ordering and Fine-Tuning of Dipole Interactions. *Small* **12**, 220-228 (2016).
141. Altantzis, T., Yang, Z., Bals, S., Van Tendeloo, G. & Pileni, M.-P. Thermal Stability of CoAu_{13} Binary Nanoparticle Superlattices under the Electron Beam. *Chem. of Mater.* **28**, 716-719 (2016).
142. Treml, B.E., Lukose, B., Clancy, P., Smilgies, D.M. & Hanrath, T. Connecting the particles in the box-controlled fusion of hexamer nanocrystal clusters within an AB_6 binary nanocrystal superlattice. *Sci Rep* **4**, 6731 (2014).
143. Yu, Y., Bosoy, C.A., Smilgies, D.M. & Korgel, B.A. Self-Assembly and Thermal Stability of Binary Superlattices of Gold and Silicon Nanocrystals. *J Phys Chem Lett* **4**, 3677-3682 (2013).

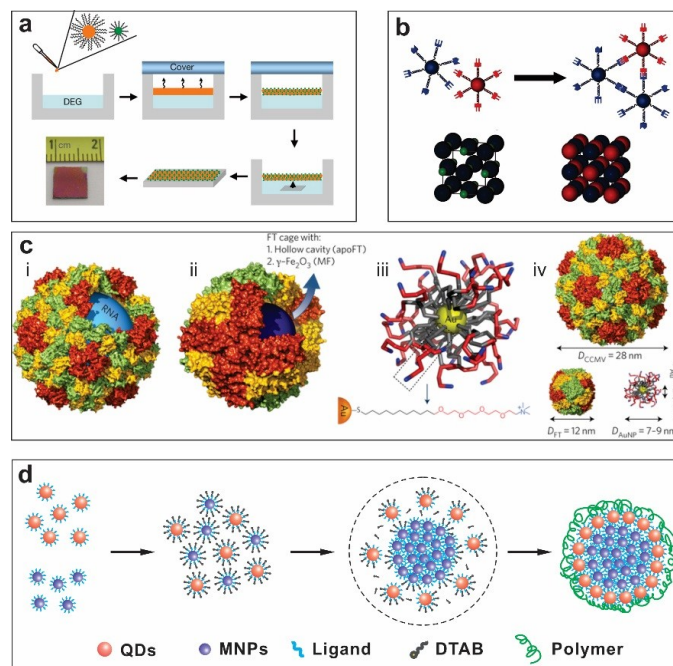


Figure 1. (a) Schematic of the BN-SL membrane growth and transfer processes. Photograph shows a typical BN-SL membrane transferred to a SiO₂-Si wafer. Mechanical damage from tweezers in the membrane's upper right corner (photo) helps visualize the scale. (b) Complex nanoparticle assemblies can be created when programming multivalent DNA-NC interactions. For example, by encoding multiple distinct sticky end sequences on NCs, both self-complementary and non-self-complementary interactions can be used to assemble lattices. Bottom: This strategy can be used to create a NaCl lattice. (c) Materials used for the assembly of binary protein cage-nanoparticle superlattices. i, Native cowpea chlorotic mottle virus with RNA genome inside. ii, Apoferritin and magnetoferritin (recombinant ferritin cage from *Pyrococcus furiosus* encapsulating Fe₃O₄-g-Fe₂O₃). iii, Au NCs stabilized with an amphiphilic ligand featuring a cationic quaternary amine end-group. iv, Size of the building blocks drawn to scale. (d) Schematic of the formation of the core-shell SPs using solvophobic interactions. Reproduced with permission from ref. 27, 34-36.

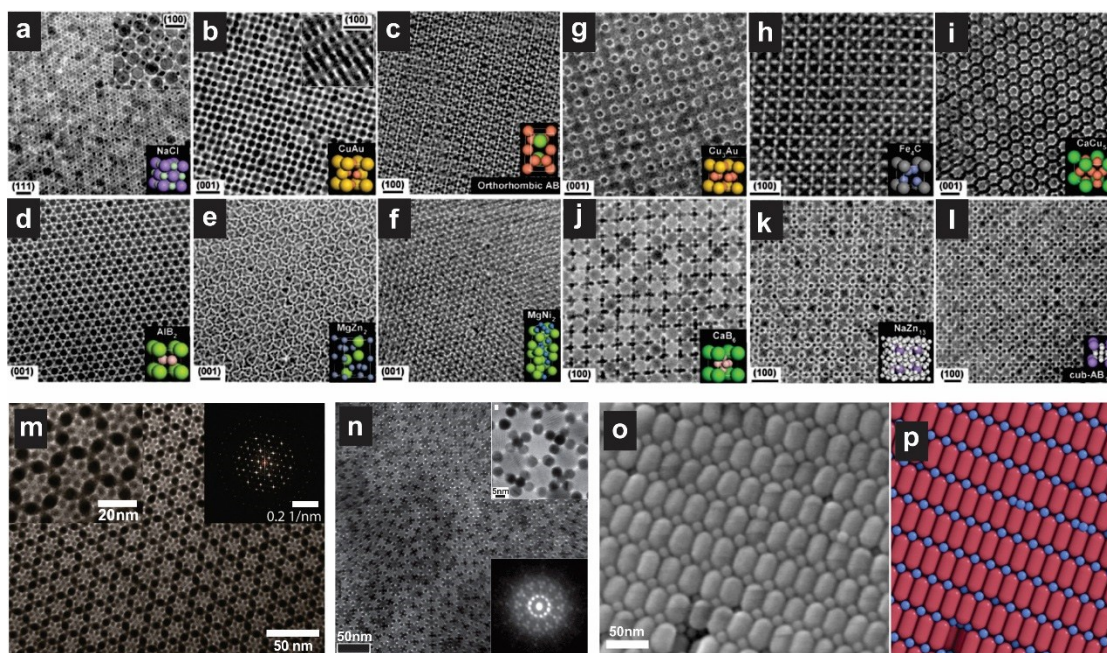


Figure 2. (a)-(l) TEM images of the characteristic projections of the BN-SLs, self-assembled from different NCs, and modeled unit cells of the corresponding 3D structures. (m) TEM image of a quasicrystalline SL self-assembled from 13.4-nm Fe_2O_3 and 5-nm Au NCs. Inset: top, magnified view of a dodecagonal NC quasicrystal; bottom, selected-area electron diffraction pattern with non-crystallographic 12-fold rotational symmetry measured from a $\sim 6\text{-}\mu\text{m}^2$ domain. (n) TEM image of NC-SL obtained in a particle size ratio 0.61-0.67 with a hexagonal symmetry. (o) SEM images of the rod-sphere self-assembled from NaYF_4 nanorods and 11.0 nm Fe_3O_4 nanospheres and (p) compared with a theoretical reconstruction. Scale bars: (a)-(c), (e), (f), (i)-(l), 20nm; (d), (g), (h), 10nm; (o) 50nm. Reproduced with permission from ref. 25, 90, 91, 95.

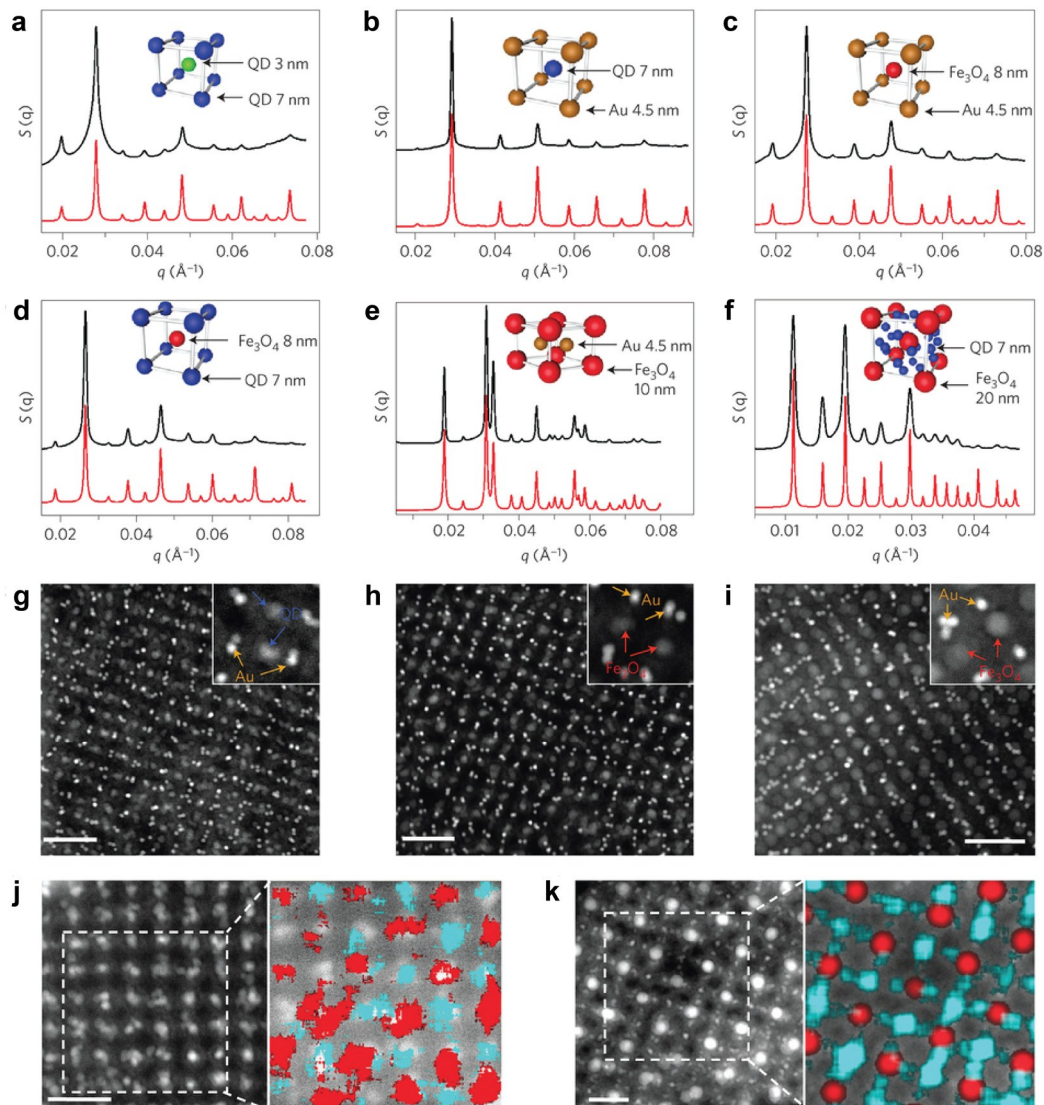


Figure 3. BN-SLs assembled from arbitrary combinations of QD-, Au- and Fe_3O_4 -Programmable atom equivalents. **(a–f)**, SAXS data for: 7nm QD, 3nm QD CsCl lattices **(a)**; 7nm QD, 4.5nm Au CsCl lattices **(b)**; 8nm Fe_3O_4 , 4.5nm Au CsCl lattices **(c)**; 8nm Fe_3O_4 , 7nm QD CsCl lattices **(d)**; 10nm Fe_3O_4 , 4.5 nm Au AlB_2 -type lattices **(e)**; and 20nm Fe_3O_4 , 7nm QD Cs_6C_{60} -type lattices **(f)**. Experimental data are shown in black, and predicted scattering patterns are shown in red. **(g–i)**, STEM images of 7nm QD, 4.5 nm Au CsCl lattices **(g)**; 8nm Fe_3O_4 , 4.5nm Au CsCl lattices **(h)**; and 10nm Fe_3O_4 , 4.5nm Au AlB_2 -type lattices **(i)**. Insets at the right corner are higher-magnification images with labels denoting particle composition. **(j)** and **(k)**, STEM images and EDX maps of 8nm Fe_3O_4 , 7nm QD CsCl lattices **(j)**, and 20nm Fe_3O_4 , 7nm QD Cs_6C_{60} lattices **(k)**. In EDX maps, the signal from Fe is shown in red, and the signal from Cd is shown in cyan. All scale bars are 50 nm. Reproduced with permission from ref. 63.

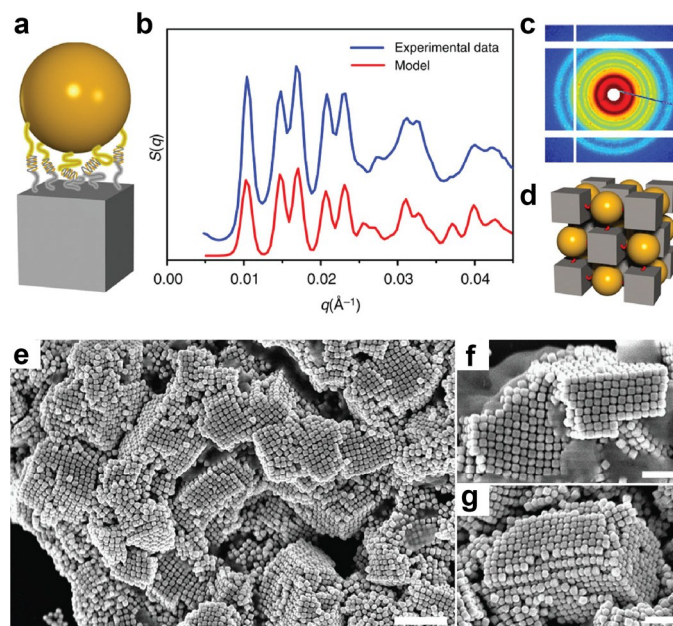


Figure 4. Cube–sphere NC assemblies of SLs. **(a)** Schematic of a 46-nm spherical NCs/46-nm cube (CB) pair linked by DNA. **(b)** SAXS data with experimental (blue) and modelled (red) structure factors, $S(q)$, **(c)** scattering image and **(d)** the corresponding structure schematic for 46-nm SNP/46-nm CB assembly system, which crystallizes into a NaCl-type lattice with a space group symmetry of $Fm\bar{3}m$. **(e)** Low-magnification SEM image of SNP/CB-assembled crystals, where square-lattice ordering can be observed from the fragments, even though drying effects caused cracks in the crystals (scale bar, 500 nm). **(f)** and **(g)** High-magnification images of superlattice, demonstrating the alternate packing of SNPs and CBs in the 3D square lattice (scale bar, 200 nm). Reproduced with permission from ref. 80.

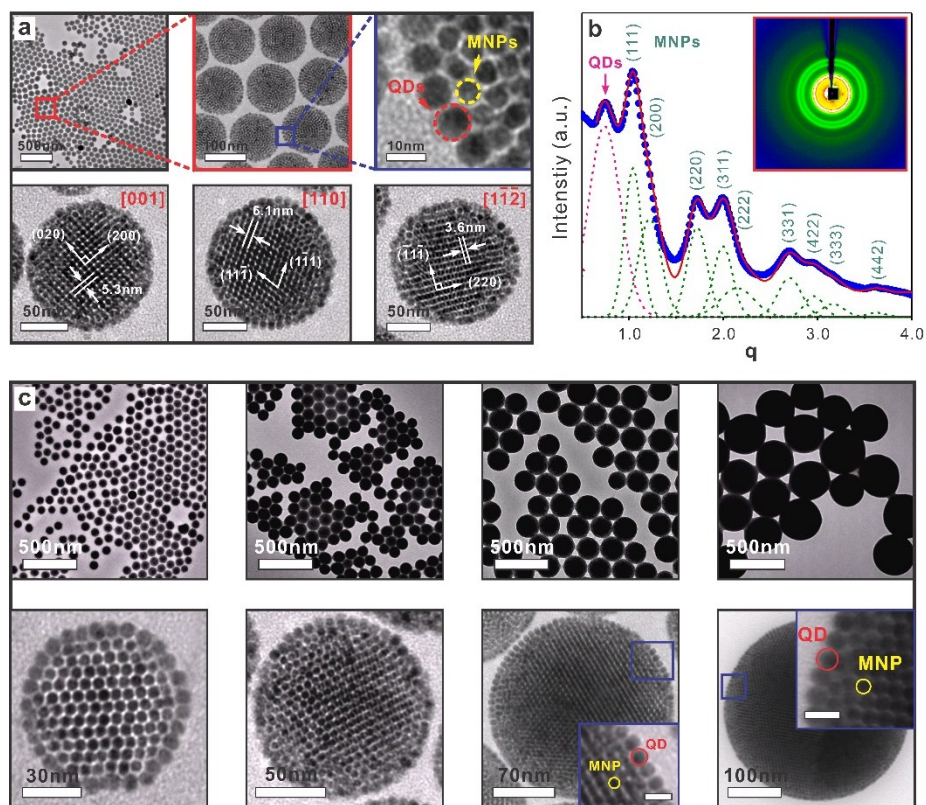


Figure 5. (a) TEM images of core-shell SPs (CS-SPs) at different magnifications and supercrystalline CS-SPs viewed along different zone axes [001], [110] and $[1\bar{1}\bar{2}]$; (b) The integrated data from the SAXS pattern (inset) of CS-SPs show a position ratio series of $q/q_0 = 1/\sqrt{4/3}/\sqrt{8/3}/\sqrt{11/3}/\sqrt{4}/\sqrt{19/3}/\sqrt{8}/\sqrt{9}/\sqrt{12}$; (q_0 is the position of the (111) peak, $q = 4\pi \sin \theta / \lambda$), indicating an fcc close packing of the MNPs. (c) Large-area and higher magnification TEM images of CS-SPs. Reproduced with permission from ref. 36.

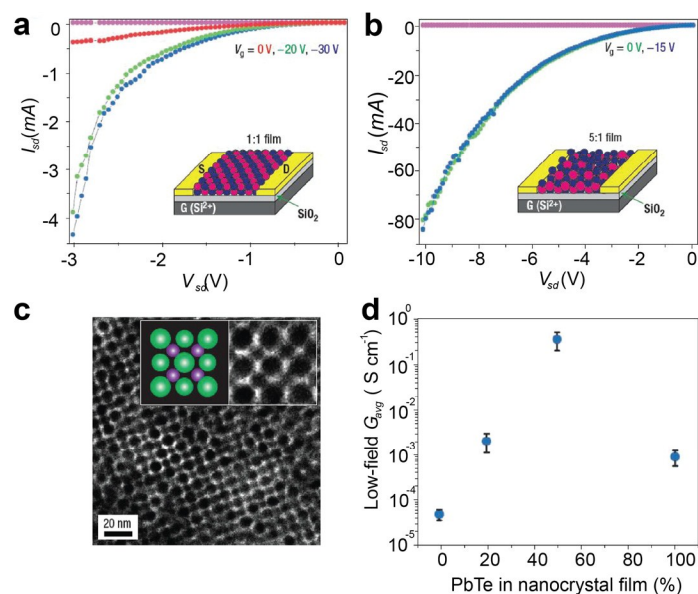


Figure 6. Characterization of binary PbTe–Ag₂Te NC films. All measurements were recorded in forward and reverse to assess device hysteresis. Gate currents (magenta) are also plotted to demonstrate that no current leakage occurred through the gate oxide. These gate currents (I_g versus V_{sd}) are recorded in parallel for each I_{sd} versus V_{sd} measurement at every gate voltage; however, owing to the low I_g values they seem collinear. (a), I – V measurement of 1:1 PbTe–Ag₂Te binary-NC film demonstrating high p-type conductivity and no gate response. (b), I – V measurement of a 5:1 PbTe–Ag₂Te binary NC film, again demonstrating p-type transport and no gate response. (c), TEM micrograph of a 1:1 PbTe–Ag₂Te SL after heat treatment, demonstrating that even 200°C thermal treatments under vacuum do not abrogate SL order. (d), Comparison of average low-field conductances (not exceeding 10 V in source–drain or 15 V in gate voltage) calculated over at least 12 devices for pure Ag₂Te films, pure PbTe films, binary 1:1 PbTe–Ag₂Te films and binary 5:1 PbTe–Ag₂Te films. The average conductance for these compositions are 5.1×10^{-5} S cm⁻¹, 9.21×10^{-4} S cm⁻¹, 0.346 S cm⁻¹ and 0.0021 S cm⁻¹, respectively. The error bars are the standard deviations in conductance values for each of the compositions. These data demonstrate the synergistic enhancement of conductivity manifest in the binary-NC solids. Reproduced with permission from ref. 37.

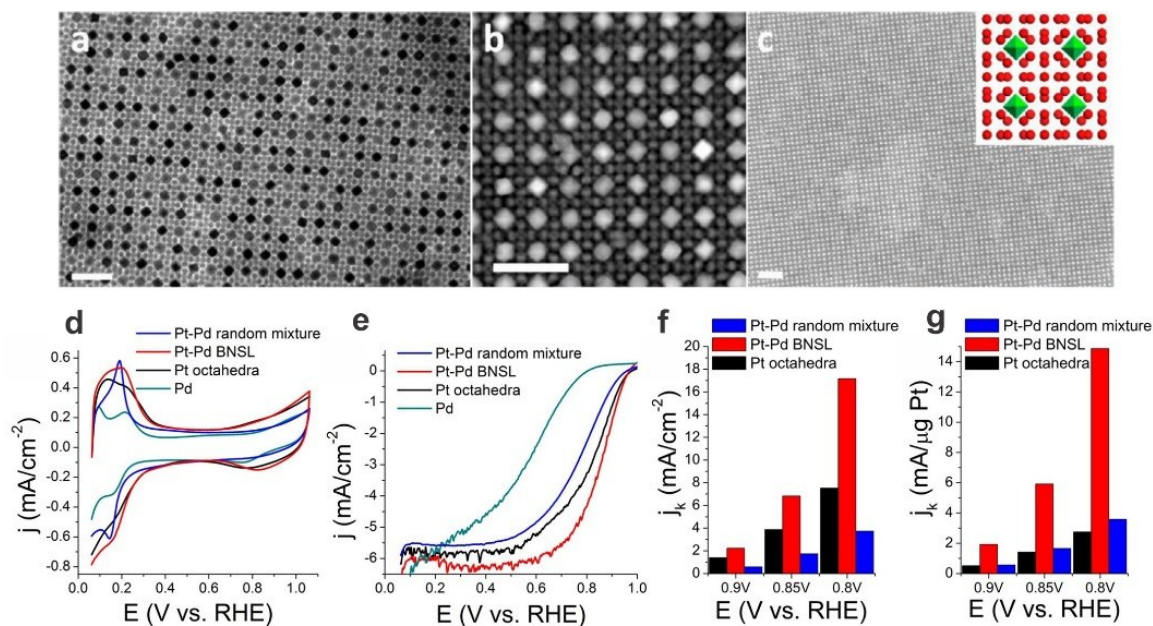


Figure 7. (a) TEM, (b) STEM-HAADF, and (c) SEM images of Pt–Pd AB₁₃-type BN-SL. (d) Cyclic voltammogram curves and (e) Oxygen reduction reaction polarization curves of a Pt–Pd BN-SL, random mixture of Pt–Pd NCs, Pd NCs and Pt octahedra. (f) and (g) Bar chart of kinetic current of Pt–Pd BN-SLs, random mixture of Pt–Pd NCs, and Pt octahedra at 0.9, 0.85, and 0.8 V. Scale bars: (a) and (b) 50nm, (c) 100nm. Reproduced with permission from ref. 96.

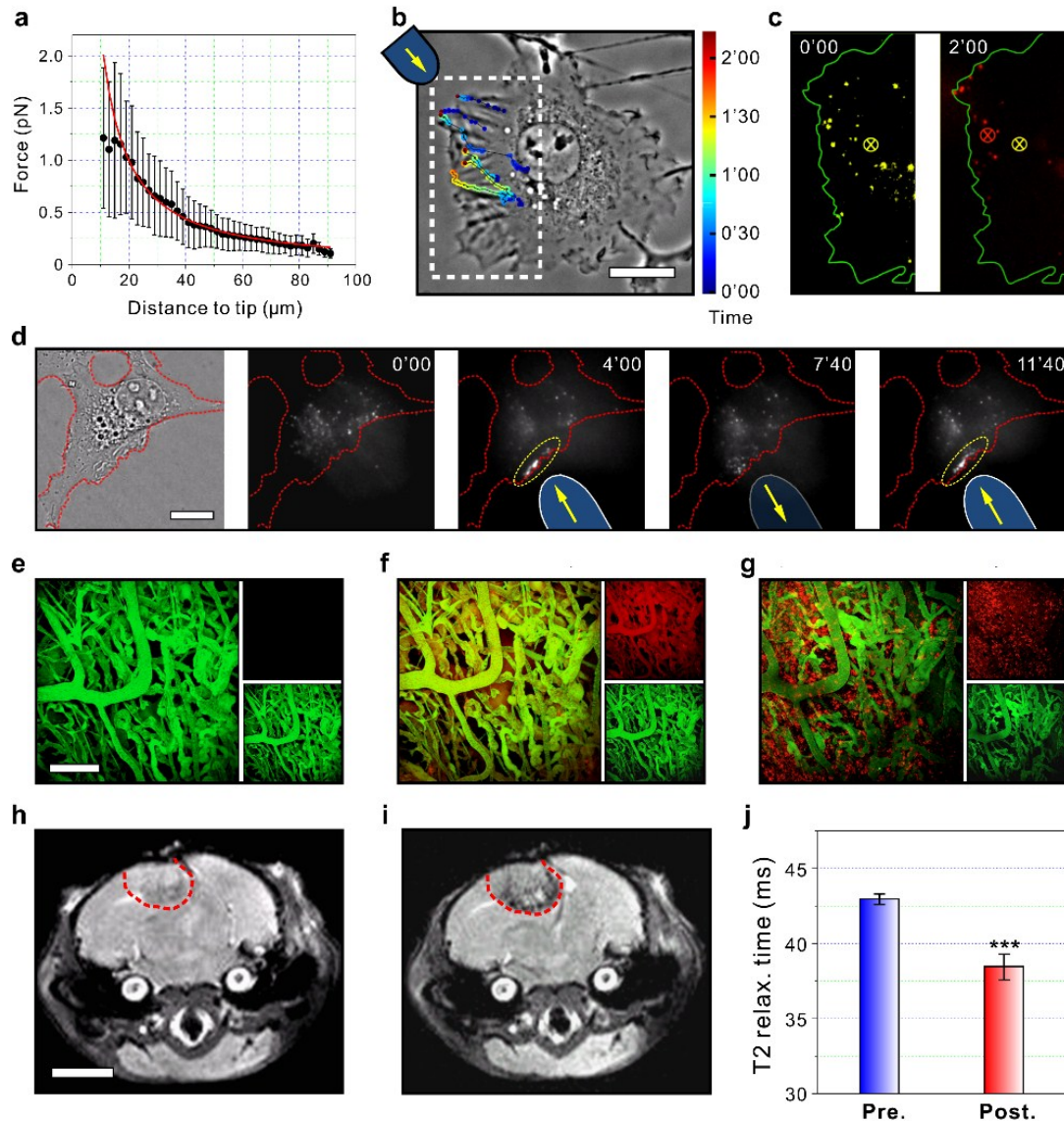


Figure 8. Silica-coated core-shell SPs (Silica-CS-SPs) in biological applications (a) Force applied to individual silica-CS-SPs as a function of the distance from the magnetic tip. A power law (red curve) fits the data. (b) Tracking of individual silica-CS-SPs during their manipulation inside a Cos7 cell. Positions along each trajectory are color-coded according to the time. Scale bar, 15 μm . (c) Left: fluorescence imaging of individual silica-CS-SPs (yellow) in the dashed line region of (b) and before the manipulation. The barycenter of the individual localizations is shown as a yellow cross. Right: superposition of the silica-CS-SPs fluorescence after 2 min (red), the barycenter of the individual localizations is shown as a red cross. (d) Left: transmission picture of a HeLa cell in which silica-CS-SPs have been microinjected. By bringing the magnetic tip in and out (blue bars), a reversible accumulation of silica-CS-SPs (yellow region) can be created at the cell periphery (indicated by red dashed line), in the direction of the magnet. Scale bar, 15 μm . mPEG-silane (MW5000) functionalized silica-CS-SPs (200 μl , 2mg/ml) were intravenously injected into C3H mice bearing brain metastasis of a murine mammary carcinoma (MCAIV) with a cranial window model. Intravital multiphoton microscopy through the cranial window was carried out at different time point: pre-injection (e), 4 h post injection (f) and 24 h post injection (g). Scale bar, 150 μm . Images from red and green channels are shown in small panels (top: red channel, bottom: green channel). Green emission signals

are generated from a blood vessel tracer (fluorescein isothiocyanate–dextran (FITC-Dextran)) and red emission signals are generated by mPEG-functionalized silica-CS-SPs. *In vivo* T2-weighted magnetic resonance images of pre- **(h)** and 24 h post- **(i)** injection of mPEG-silane functionalized silica-CS-SPs. Twenty four hours post-injection image show clear tumor visualization (denoted by the red dash line). Scale bar, 3 mm. **(j)** The corresponding T2 relaxation (relax.) time fitting results for the tumor region at time points of pre-injection (Pre., blue bar) and 24 h post injection (Post., red bar). n=5 mice, *** P<0.001 (Student's t-test). Reproduced with permission from ref. 36.

Acknowledgements

O.C. acknowledges support from Brown University startup.

Note

§ These authors contributed equally to this work